Article

Effect of Ethylene Glycol:Citric Acid Molar Ratio and pH on the Morphology, Vibrational, Optical and Electronic Properties of TiO$_2$ and CuO Powders Synthesized by Pechini Method

Mónica A. Vargas-Urbano [1,2], **Lorena Marín** [3,4,*], **Winny Mónica Castillo** [3], **Luis Alfredo Rodríguez** [1,3], **César Magén** [5,6], **Milton Manotas-Albor** [7], **Jesús Evelio Diosa** [1,3] **and Katherine Gross** [3,4]

[1] Grupo de Transiciones de Fase y Materiales Funcionales (GTFMF), Departamento de Física, Universidad del Valle, A.A. 25360 Cali, Colombia; vargas.monica@correounivalle.edu.co (M.A.V-U.); luis.a.rodriguez@correounivalle.edu.co (L.A.R.); jesus.diosa@correounivalle.edu.co (J.E.D.)

[2] Grupo CYTEMAC, Departamento de Física, Universidad del Cauca, Popayán, Colombia; monicavargas@unicauca.edu.co (M.A.V-U.)

[3] Centro de Excelencia en Nuevos Materiales (CENM), Universidad del Valle, A.A. 25360 Cali, Colombia; marin.lorena@correounivalle.edu.co (L.M.); winny.castillo@correounivalle.edu.co (W.M.C.); luis.a.rodriguez@correounivalle.edu.co (L.A.R.); katherine.gross@correounivalle.edu.co (K.G.); jesus.diosa@correounivalle.edu.co (J.E.D.)

[4] Grupo de Película Delgadas (GPD), Universidad del Valle, A.A. 25360 Cali, Colombia; marin.lorena@correounivalle.edu.co (L.M.); katherine.gross@correounivalle.edu.co (K.G.)

[5] Instituto de Nanociencia y Materiales de Aragón (INMA), Departamento de Física de la Materia Condensada, Universidad de Zaragoza, 50009 Zaragoza, Spain; cmagend@unizar.es (C.M.)

[6] Laboratorio de Microscopias Avanzadas (LMA), Universidad de Zaragoza, 50018 Zaragoza, Spain; cmagend@unizar.es (C.M.)

[7] Grupo de Investigación en Física Aplicada (GIFA), Departamento de Física y Geociencias, Universidad del Norte, Barranquilla, Colombia; manotasm@uninorte.edu.co (M. M-A)

* Correspondence: marin.lorena@correounivalle.edu.co; Tel.: +57 3167696970

Abstract: High purity TiO$_2$ and CuO powders were synthesized by the Pechini method, an inexpensive and easy-to-implement procedure to synthetize metal oxides. The variables of synthesis were the ethylene glycol:citric acid molar ratio and the pH. High reproducibility of the anatase and tenorite phase was obtained for all synthesis routes. The degree of purity of the powders was confirmed by XRD, FTIR, UV-vis absorption and XPS spectra. SEM and TEM images revealed the powders are composed by micrometer grains that can have a spherical shape (only in the TiO$_2$) or formed by a non-compacted nanocrystalline conglomerate. FTIR spectra only vibrational modes associated to the TiO$_2$ or CuO with a nanoparticle behavior. UV-vis absorption spectra revealed the values of maximum absorbance percentage of both systems are reached in the ultraviolet region, with percentages above 83 % throughout the entire visible light spectrum for the CuO system, a relevant result for solar cell applications. Finally, XPS experiments allow the observation of the valence bands and the calculation of the energy bands of all oxides.

Keywords: Pechini method; TiO$_2$; CuO; anatase; tenorite; band gap; absorbance; diffuse reflectance; XPS

1. Introduction

Great efforts have been made over the years to control the photophysical and photochemical properties of metal oxides at the micro- and nanoscale, being the synthesis procedure a crucial factor in controlling crystalline structure, particle size and morphology [1,2]. An ongoing quest of the scientific community is discovering the ways in which the synthesis might influence the optical and electronic properties of these materials. Metal oxide-based semiconductor materials have been obtained using different methods, including chemical vapor synthesis [3], sol-gel [4,5], hydrothermal [6], controlled precipitation [7], and polymeric precursor [8]. The polymeric precursor method, commonly named

as Pechini method, is one of the most economical and easily implemented methods to produce metal complexes from concentrated solutions of polyfunctional organic acids, salts or oxides of the cations required for the formation of metal oxides [9]; it combines low-temperature processing and versatility in the proportions of citric acid and metal cations to control the stoichiometry and the morphology of the particles and/or agglomerates, obtain compositional homogeneity and ensure low toxicity to produce a single-phase nanometric powder [10,11].

To produce multifunctional oxides such as titanium dioxide (TiO_2) and copper II oxide (CuO) by Pechini method, titanium tetrabutoxide and copper acetate are respectively used as concentrated solutions, and two basic chemical reactions are involved: the formation of a chelating complex composed of carboxylic acid, chelating agent and metal matrix, followed by its polyesterification with excess polyalcohol [10], giving rise to a viscous resin [9,11]. Continued heating of the solution causes distillation of all the water and carboxylic acid, resulting in the polymer. The decomposition of this resin, commonly amorphous, is carried out by calcining it at temperatures below 300 °C. With this synthesis method, the problems of segregation or preferential precipitation in the solution are overcome because the cations are fixed to the resin, thus allowing greater control of the stoichiometry of the compound to be synthesized. The reagents commonly used in applying this method are citric acid (CA) and ethylene glycol (EG) [10,12]. Pechini reported 4:1 as the optimal EG:CA molar ratio [11], however, these synthesis parameters have been varied to study the effect on the morphology and thus the change in the optical and electronic properties of oxides such as TiO_2 [13], CuO [14] and ZnO [15]. The literature indicates that the structural characteristics of the semiconductor oxides can be controlled through the parameters of synthesis, depending on the technological applications desired. These include the fields of optics, electronics, and telecommunications, as well as a strong representation in the field of chemistry, where they have been used as electrodes in voltaic and electrolytic cells, magnetic recording medium, anode material for lithium-ion batteries, gas sensors, antibacterial agents, and catalyst materials [15–18]. In general, the different technological applications of these materials lie in their potential to be used in photovoltaic devices [19], whose operating principle is based on the generation of electric current as a consequence of the absorption of light with an energy equal to or greater than the band gap (E_g) of the material [20], requiring that the E_g be comparable to the energy of photons of visible or ultraviolet light, that is, that it has a value of $E_g < 3.5$ eV [21].

In this work, we selected TiO_2 and CuO due to their E_g values, which are found in the ultraviolet and visible spectrum. There are three crystalline forms of TiO_2: anatase, rutile, and brookite. The anatase phase is metastable and has the highest photocatalytic activity, so in our study, we will synthesize and analysis this phase. It has a direct band gap transition value of 3.2 eV [22,23]; although indirect band gap transitions in the range of 2.86 to 3.34 eV have also been reported [24], where its differences are attributed to variations in the stoichiometry of synthesis, impurity content, crystal size and type of electronic transition [21,24]. The tenorite (CuO) is a p-type semiconductor that has received a lot of attention since the discovery of high-temperature cuprate superconductors. However, its electronic structure has not been fully resolved and there are reports in the literature of direct [2,25] or indirect [25-27] E_g transitions. Here, several physical properties were analyzed based on two variables of synthesis: EG:CA molar ratio and pH.

2. Materials and Methods

2.1. Synthesis of the CuO and TiO_2

Powders of TiO_2 and CuO were synthesized by the Pechini method following four different routes that involved two types of molar ratios of the polymerization mixture (2:1 and 4:1), with two different pHs (8 and 9), routes referred to henceforth as 2:1 pH8, 2:1 pH9, 4:1 pH8 and 4:1 pH9. In the first stage of the process, ethylene glycol (Merck) was heated on a hotplate at 70 °C and then the correct amount of citric acid was added to

ensure a molar ratio of EG:CA of 2:1 and 4 :1, ratios that have been previously used to synthesize TiO_2 and CuO [10,14,28]. After the citric acid completely dissolved in the ethylene glycol, the mixture was allowed to cool to room temperature, when the precursor of the oxide of interest was added to the mixture: $Ti(OCH_2CH_2CH_2CH_3)_4$ (Sigma Aldrich) and $Cu(CO_2CH_3)_2$ (Sigma Aldrich) to produce TiO_2 and CuO, respectively. The new mixture was maintained under constant stirring for several minutes until completely transparent to avoid phase segregation during the oxide synthesis process. To bring the mixture to a basic pH of 8 and 9, ammonium hydroxide (NH_4OH) (Merck) was added at low stirring speed (see Figure S1, supplementary information). This final mixture was heated at 140 °C, on a hotplate, to eliminate the solvent and favor the polyesterification reactions, which produce a resin. Finally, this resin was calcined in an oven at a temperature of 300 °C for 3 hours to obtain an intermediate solid material with a high content of organic material. To determine the precalcination and sintering temperatures of the oxides, a thermal study was carried out by differential scanning calorimetry (DSC) and thermogravimetric analysis (TGA) (see Figure S2, supplementary information), finding that both oxides can be crystallized with a thermal treatment at 450 °C for 4 hours, in an air atmosphere.

2.2. Characterization techniques

Identification of the crystalline phases present in the powders of the synthesized oxides was carried out by means of the analysis of high-resolution X-ray diffractogram (XRD) scans taken in a Bruker D8 ADVANCE ECO equipment, with a Cu anode (λ = 0.1540 nm) and an operating voltage of 40 kV. The diffractogram scans were taken in powder mode, with a step size of 0.01°, in the range of 10° to 100°. To determine the morphology of the powders, scanning electron microscopy (SEM) images were taken in a FEG INSPECT-F50 equipment. A more detailed analysis, with higher spatial resolution, of the TiO_2 and CuO grains was performed using high-resolution transmission electron microscopy (HRTEM) images, taken on a FEI-Titan Cube 60-300 microscope, operated at 300 kV and equipped with a SuperTwin® objective lens and a CETCOR spherical aberration corrector (CEOS company) that facilitates spatial resolutions of 0.08 nm.

For the qualitative determination of the functional groups, infrared spectroscopy (FTIR) experiments were performed using a Thermo Scientific Nicolet FTIR6700 infrared spectrometer to measure transmittance as a function of wavelength of the light source, sweeping a range from 400 to 4000 cm^{-1}. To determine the E_g, diffuse reflectance spectra (UV-DRS) were taken at room temperature using a JASCO V-750 spectrometer, equipped with an integrating sphere in a range of 200 to 2500 nm. The chemical nature and the binding energy (BE) were investigated by X-ray photoelectron spectroscopy (XPS), using an XPS Spectrometer Kratos AXIS Supra equipment.

3. Results

3.1. Structural and morphological analysis

3.1.1. X-ray diffraction

Figure 1 shows the powder XRDs of the synthesized TiO_2 and CuO. All the diffractograms present narrow and well-defined peaks, suggesting that both oxides have been synthesized with a high degree of crystallinity [14]. In addition, a visual comparison between the XRDs allowed us to conclude that all four synthesis routes showed the same crystalline microstructure for each type of oxide. On performing an XRD analysis by indexing the representative peaks, we found that all four synthesis routes allowed TiO_2 to crystallize in its anatase phase (PDF 21-1272), without traces of secondary phases such as the rutile TiO_2, a phase that usually appears when using ethylene glycol:metal cation molar ratios of 3:1 and 4:1 [10]. In the case of CuO, we find how its monoclinic structure was crystallized (PDF 80-1916), also free of secondary phases. These results show that the dif-

ferent routes of the Pechini method used in this work made it possible to obtain the desired phases of TiO_2 and CuO, virtually pure within the resolution limits of the XRD technique.
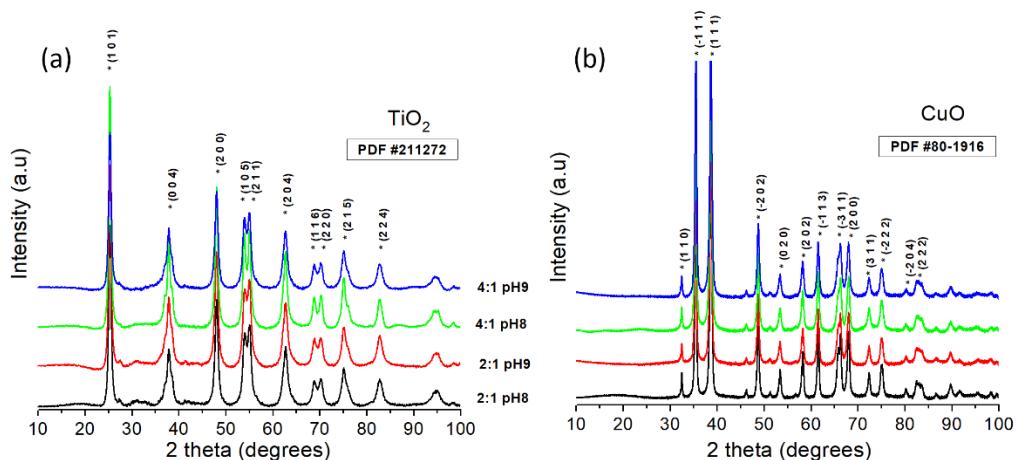

Figure 1. X-ray diffractograms for the (a) TiO_2 and (b) CuO powders synthesized using the four Pechini method routes.

3.1.2. Scanning and transmission electron microscopy

SEM images taken at 20.000x magnification of synthesized TiO_2 powders are shown in Figures 2(a)-(d). In all cases, it observes that TiO_2 powders were synthesized following two main types of morphologies: (*i*) grains with irregular shapes and sizes, ranging from several microns to tens of nanometers and (*ii*) submicron spheres. In addition to these grains, small crystallites with sizes of tens of nanometers can be observed on the grains surface. In the case of the spheres, we notice how these tend to agglomerate; some of them are perfectly defined, while others seem to be linked together. By selecting between 20 and 30 spheres from the SEM images, a diameter distribution analysis was carried out according to the different routes by using a lognormal distribution function to adjust the histograms (see Figure 2(c)). The distribution fittings show us that the spheres grown with the 2:1 molar ratio (2:1 pH8 and 2:1 pH9) have similar mean diameters (734 and 770 nm, with standard deviations of 125 and 143 nm, respectively) which reflects that, in general, the pH variation did not produce significant changes in diameter. However, for the TiO_2 spheres grown with the 4:1 molar ratio, we clearly see a difference between the mean diameter: while the spheres grown with pH 9 have mean sizes similar to those grown with the 2:1 ratio (745 nm, with a standard deviation of 112 nm), reducing the pH to 8 produced spheres with a larger mean diameter (1007 nm, with a standard deviation of 168 nm). Thus, the SEM analysis of the synthesized TiO_2 reveals the resulting powders are mainly formed by micrometer- and submicrometer size grains, without a clear dependency with the synthesis route followed in this work. It is important to highlight that our Pechini-based synthesis routes achieve to produce submicrospheres, similar to those synthesized by simple solution and sol-gel methods [29-32], a particular geometry that provides structural and electronic properties suitable for application that require high absorbate binding energy for the functionalization of nanoparticles [33].

SEM images taken at 100,000x magnification of synthesized CuO powders are shown in Figures 3(a)-(d). Their morphology is completely different from that observed in TiO2 powders. The CuO2 grains seem to be composed of non-compact crystallite conglomerates. A visual comparison allows us to assume that the crystallite conglomerates have larger sizes in the CuO grains grown with a 4:1 molar ratio. However, it is difficult to conclude such a fact due to their irregularity.
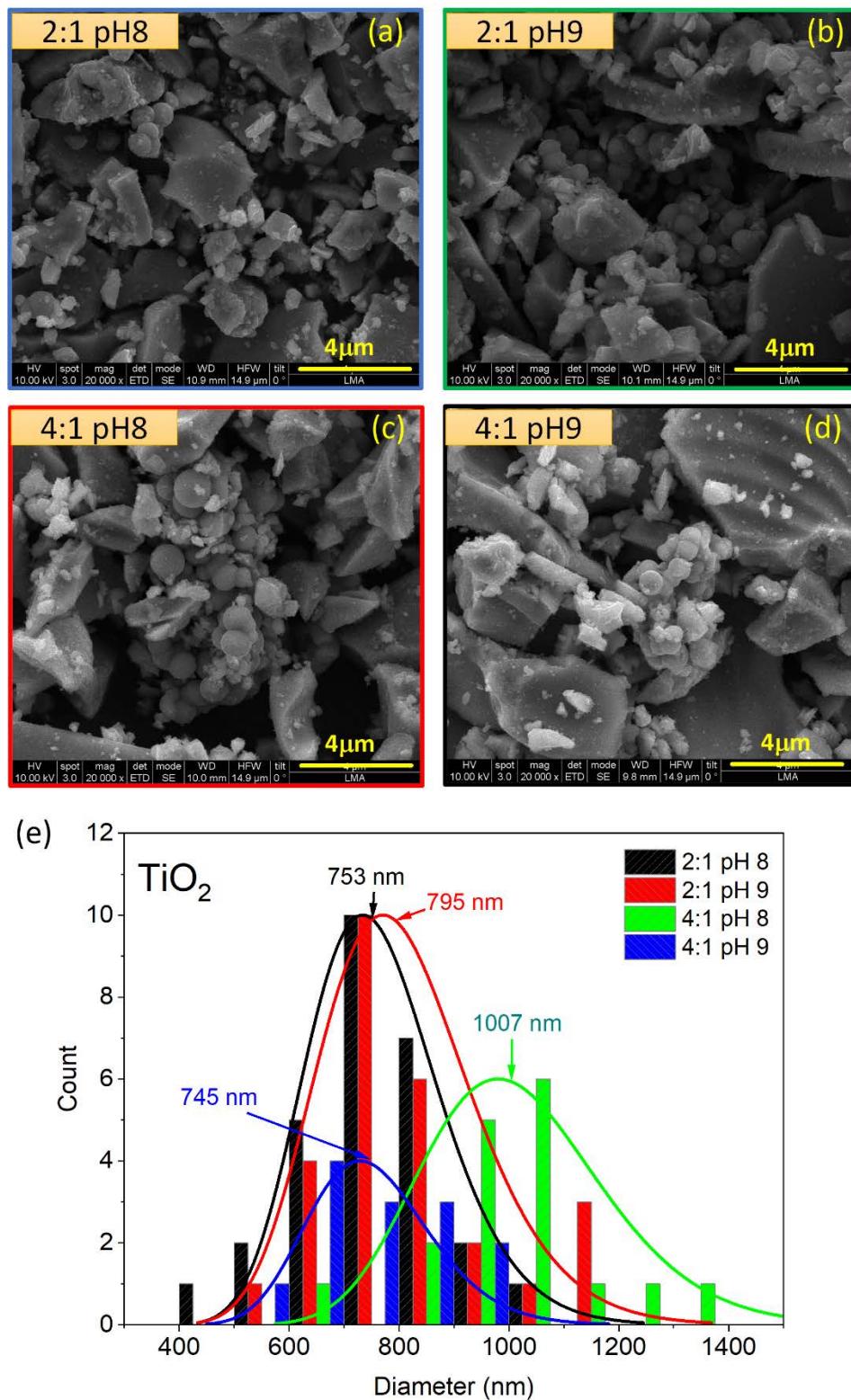
Figure 2. SEM images taken on TiO_2 powders grown with the molar ratio + pH (a) 2:1 pH 8, (b) 2:1 pH 9, (c) 4:1 pH 8 and (d) 4:1 pH 9. (e) Histograms of diameter distributions of the spheres. Lines correspond to the lognormal distribution fittings.
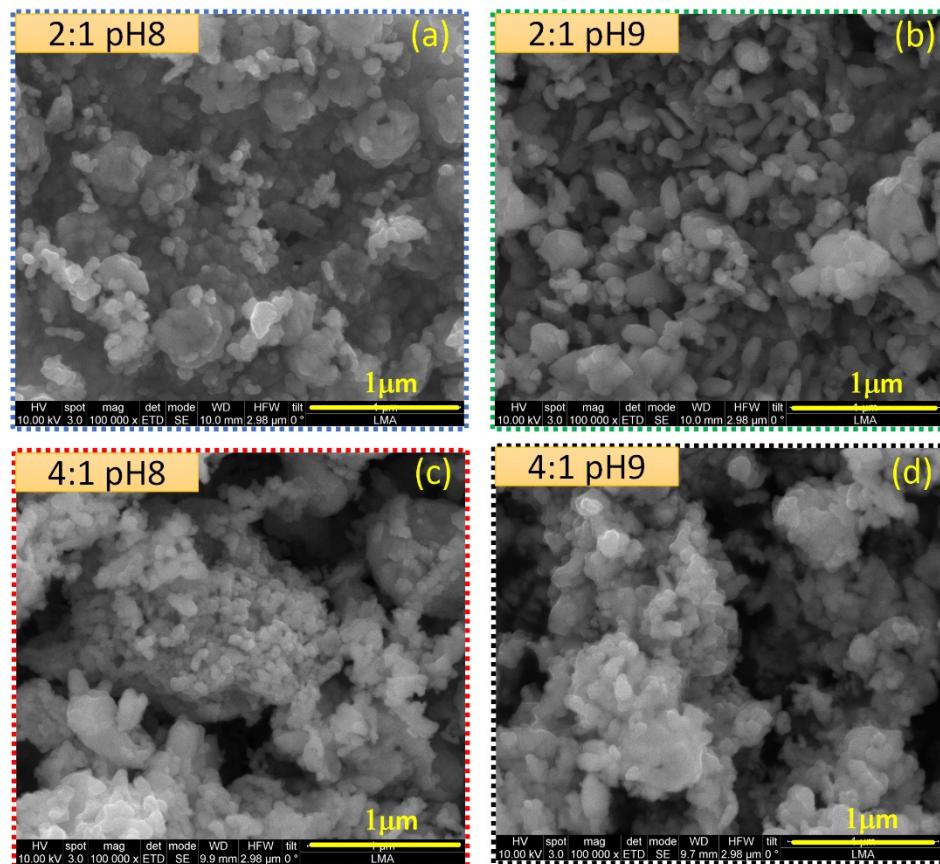
Figure 3. SEM images taken on CuO powders grown by following the (a) 2:1 pH 8, (b) 2:1 pH 9, (c) 4:1 pH 8 and (d) 4:1 pH 9 synthesis routes

A series of TEM images taken on representative TiO2 and CuO grains are displayed in Figures 4 and 5. Due to the great morphological similarities of the TiO2 and CuO powders synthesized in each of the routes, here we will only show TEM images for TiO2 and CuO nanostructures obtained by the 2:1 pH8 route. Figure 4(a) and (b) show TEM images of the two types of grains observed through the SEM images of TiO2 powders: spherical grains with diameters between 648 and 918 nm, and an irregularly shaped grain with an average size close to 1 μm. An HRTEM image, taken at the surface of the grain shown in Figure 4(b), is shown in Figure 4(c) and reveals that the irregularly shaped grains are composed of small crystallites that are a few tens of nanometers in size. In this image, we can see that the crystallites do not exceed 20 nm in size and seem to form a non-compacted grain. A diffraction image digitally obtained from the HRTEM image in Figure 4(c) shows that the nanocrystallites produce diffraction rings (see Figure 4(d)), which allows us to conclude that they are randomly oriented along the grain. On the other hand, as we see in Figure 5(a), the CuO grains are composed by crystallites that have sizes much larger than those observed for the TiO2 grain. Here we find, for instance, crystallites that can have average sizes greater than 100 nm. On comparing with the SEM images, we see that these nano- and submicro-meter crystallites induce the formation of grains composed of conglomerates of non-compact crystallites. In some crystallites, it can be noted how a submicron size induces the formation of dislocations during the crystallization process. To illustrate this, Figure 5(b) shows a high-magnification TEM image of a crystallite that possesses two antiphase boundary dislocations.
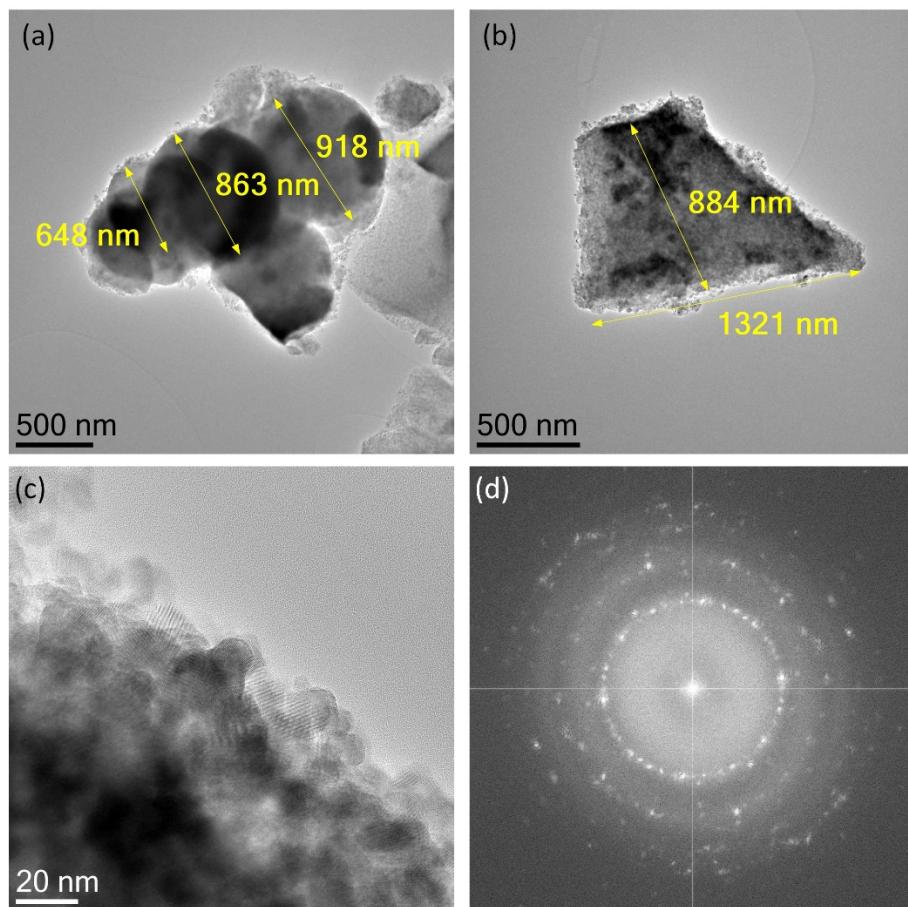
Figure 4. TEM images taken of (a) a conglomerate of submicron TiO_2 spheres and (b) an irregular TiO_2 grain crystallized by the 2:1 pH8 synthesis route. (c) HRTEM image recorded at the grain surface of (b). (d) Diffraction image digitally obtained from (c) after applying a fast Fourier transform.
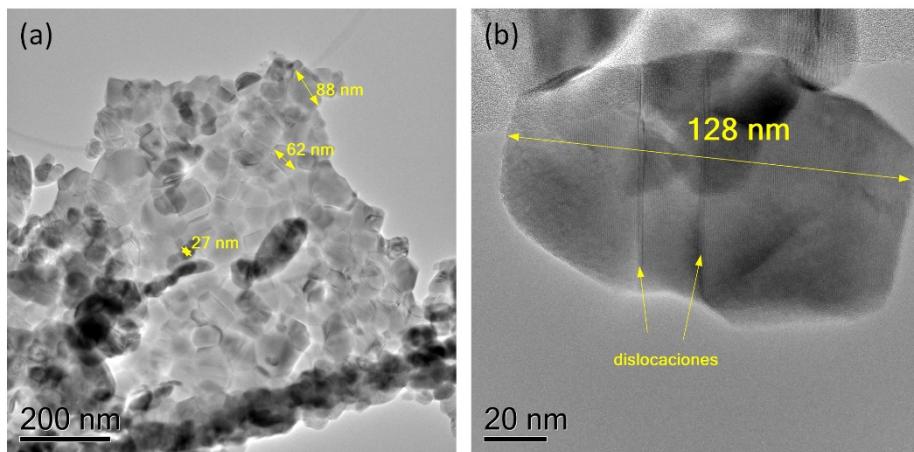

Figure 5. (a) TEM images taken of a CuO grain composed by a crystallite conglomerate and synthesized by the 2:1 pH8 synthesis route. (b) HRTEM image taken of a CuO crystallite with dislocations.

3.2. Characterization of vibrational properties

3.2.1. FTIR spectroscopy

FTIR spectra taken from the TiO2 and CuO powders, synthesized by the four routes, are presented in Figure 6. In the case of TiO2, a visual inspection of the spectra indicates that there are no significant variations between them (see Figure 6 (a)), so that the vibrational properties of TiO_2 powders are not altered by the synthesis route followed in this

work. We see that the spectra only present a broad band in the range of 500 to 1000 cm^{-1}, a region in which the anatase phase of TiO$_2$ shows its characteristic peaks [34,35], reflecting the high purity with which this oxide was synthesized, a result consistent with the XRD observations. Additionally, the shape of this band, wide and with two small minima associated with vibrations due to stretching of the Ti-O and Ti-O-Ti bonds, indicates that the TiO$_2$ powders, despite being made up of conglomerates of nanocrystallites, have a vibrational behavior typical of nanoparticles [36-41] or nanocrystalline mesoporous powders [42], a spectrum that differs from that found in commercial powders and nanorods, which have well-defined peaks, or a noisy spectrum within the range between 400 and 1000 cm^{-1} [43-45]. In a comparable way to TiO$_2$, the FTIR spectra taken of CuO powders show only representative peaks in the range of 500 and 625 cm^{-1}, a region in which CuO presents its vibrational modes, thus demonstrating its high purity and nanoparticle vibrational behavior [14]. The bands located at 547 cm^{-1} and 590 cm^{-1} related to the vibrations of the Cu–O functional group [36,46,47] are identified. While the 590 cm^{-1} band is defined for the four CuO samples, the 547 cm^{-1} band cannot be identified for the 4:1 EG:CA molar ratio (see Figure S3, supplementary information).
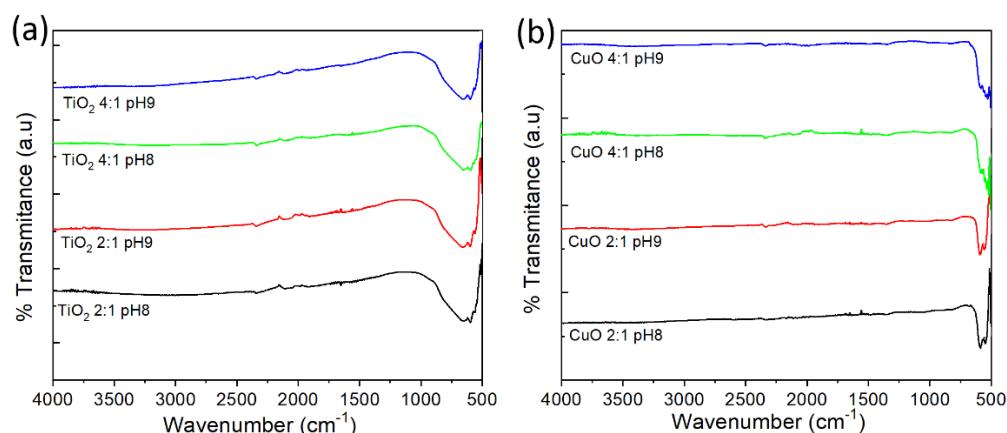

Figure 6. FTIR spectra for the powders of (a) TiO$_2$ and (b) CuO synthesized using the four Pechini-based synthesis routes.

3.3. *Characterization of photophysical properties*

3.3.1. UV-Vis spectroscopy

The optical properties of the samples were studied from ultraviolet-visible (UV-Vis) absorption spectra performed in a wavelength range from 200 to 2500 nm (See Figure 7), at room temperature. As we see in Figure 7(a), the absorption spectra for all synthesized TiO$_2$ powders show that the absorbance significantly increases for values below 700 nm, reaching a maximum intensity around 352 nm wavelength, which ranging between 75 % (for 2:1 pH 8) and 84 % (for 4:1 pH 9). In the UV region (inset of Figure 7(a)), three absorption bands around 212, 237 and 352 nm are distinguished, which are characteristic of TiO$_2$ nanoparticles [48]. Moreover, we observe an increasing dependence of the absorbance percentage with EG:CA ratio, as well as with the pH, which is remarkable for the 2:1 ratio and almost imperceptible for the 4:1 ratio. Finally, it should be noted that, in the visible range, the TiO$_2$ powders grown by 4:1 pH8 route shows the greatest absorption capacity, presenting 28% and 50 % in red and violet lights, respectively, while the rest of the powders present an absorption below 15% in red light.
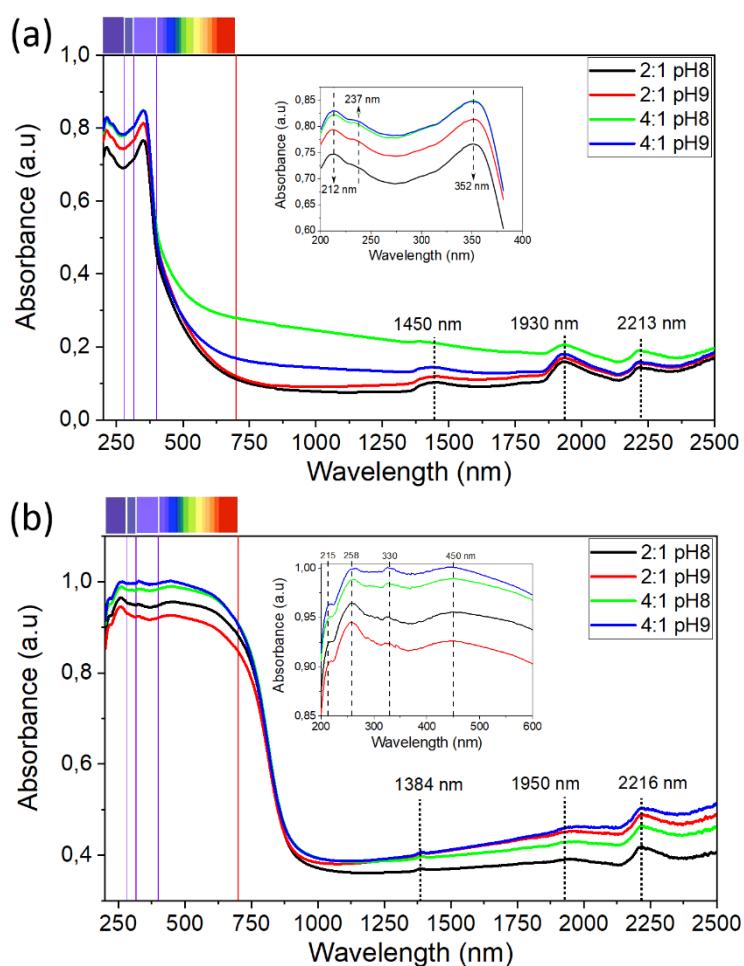
Figure 7. UV-Vis absorption spectra of the studied (a) TiO₂ and (b) CuO powders. The inset of each figure is a zoom-in of the spectra in the UV region.

The UV-Vis absorption spectra of all CuO powders (see Figure 7(b)) exhibit the highest absorbance percentages in the visible and ultraviolet regions, reaching a maximum intensity in the around 258 nm wavelength. In the 200-450 nm region, four absorption bands around 215, 258, 330 and 450 nm are distinguished (inset of Figure 7(b)). In terms of the EG:CA ratio, and pH for the 4:1 ratio, the absorption spectra of the CuO powders show a similar increasing tendency than that found in the TiO₂, however there is decreasing tendency with the pH for the 2:1 ratio. It should be noted that in the visible range, all CuO samples have an absorbance greater than 83 %. Finally, the absorption peaks observed around 1450 – 1384, 1950 - 1930 and 2216 - 2213 nm are produced by the instrument to test the spectrum curves [25,49].

To extract Eg for all oxides, the Kubelka-Munk method is applied on diffuse reflectance curves obtained from the UV-Vis absorption spectra [50]. Here we plot $[f(r)hv]^2$ as a function of the photon energy (hv), being f(r) the Kubelka-Munk function (see Figure S4, supplementary information). According to the linear extrapolation fits carried out on the diffuse reflectance curves, we obtained the direct E_g value for the TiO₂ around 3.2 eV (see Figure 8), being it the same for all powders (see inset of Figure 8(a)). In the case of the direct E_g values estimated for the CuO powders, they fluctuate around 1.5 eV; while the 2:1 pH8 and 2:1 pH9 samples tend to have a slightly lower value than 1.5 eV, the 4:1 pH8 and 4:1 pH9 samples tend to be slightly higher. Both TiO₂ and CuO powders showed values close to the theoretical 3.2 eV [51-53] and 1.45 – 157 eV [54], respectively, both showing direct band semiconductor behavior, an ideal result to improve absorption efficiency of

the solar energy in photovoltaic devices [22]. Table 1 lists the optical band gap values of all samples.
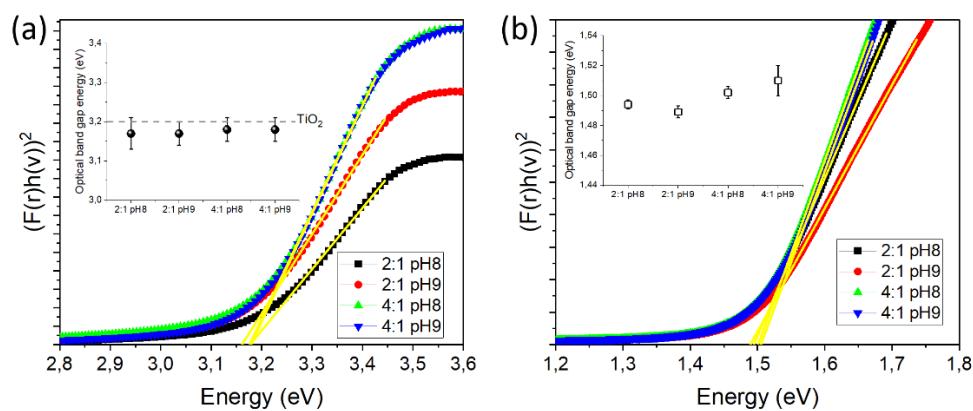

Figure 8. Curves of Kubelka-Munk function against absorbed light energy for the studied (a) TiO$_2$ and (b) CuO powders. In the insets, a plot of Eg values as a function of the synthesis route, for each oxide, is shown. The dotted line in the inset of (a) indicates the theoretical value of bulk TiO$_2$.

3.3.2. XPS measurements

To estimate the oxidation states and the valence band energy (E_{VB}) of the powders, XPS experiments were performed. The spectra were taken from a broad sweep of energies, from 0 to 1200 eV (see Figure S5, supplementary information), but we have focused our analysis in very narrow and specific regions. Figure 9 shows high-resolution XPS spectra taken around characteristic peaks of the TiO$_2$ and CuO systems. Figure 9(a) shows the Ti 2p peaks for the TiO$_2$ system, where the expected doublet (Ti 2p$_{3/2}$ and Ti 2p$_{1/2}$) is detected. The BE of the peaks are 458.7 (Ti 2p$_{3/2}$) and 464.5 eV (Ti 2p$_{1/2}$), and are associated to the Ti(IV) oxide [55]. Figure 9(b) shows a comparison of the Cu 2p$_{1/2}$ regions, observing a maximum of the Cu 2p$_{3/2}$ signal at 933.8 eV and presenting the characteristic satellite profile reported for Cu(II). Specifically, both the BE recorded in the samples and the spectra profile correspond to what is expected for our anatase and tenorite phases [56]. In both oxides, there is not a spectra variation with the synthesis routes.
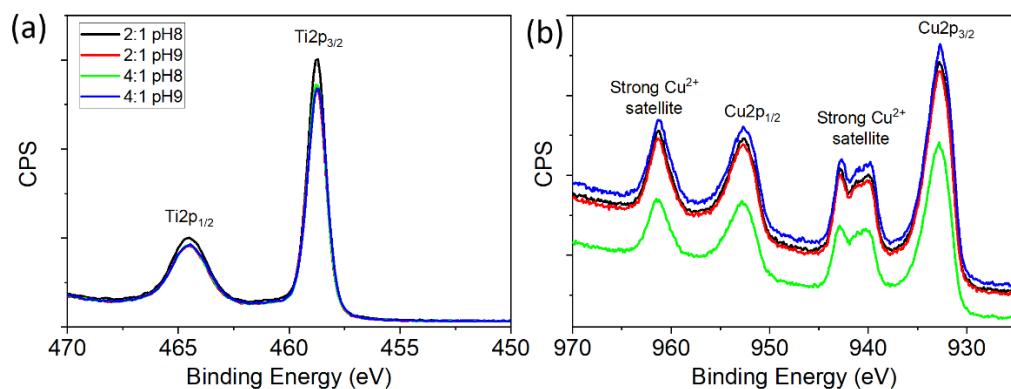

Figure 9. XPS spectra of the (a) Ti 2p and (b) Cu 2p peaks for the TiO$_2$ and CuO powders, respectively.

Figure 10 shows the XPS spectra of the low-binding energy electrons as well as XPS valence band spectra of all powders. While the TiO$_2$ powders exhibit a valence band with a well-defined maximum energy edge, located above the Fermi level (E_F, it has BE = 0),

the CuO powders present a distorted valence band with a small band tail that has a negative energy edge. The presence of a band tail in XPS valence band spectra of CuO has been reported [57-60], it is caused by defects in disordered regions of the system, mainly located at the surface, that promote the electron hybridization. From XPS valence bands, we estimated E_{VB} by performing a linear extrapolation to zero counts per second (CPS) around the maximum energy edge. All synthesized TiO_2 powders have the same $E_{VB} = 2.6$ eV, value that is in good agreement with that reported in the literature [61]. On the other hand, most of the CuO powders have a maximum E_{VB} (E_{VB-max}) of around 0.98 eV, and a minimum E_{VB} (E_{VB-min}) close to -0.51 eV, the later determined from the band tail. Only the CuO powder synthesized by 4:1 pH9 route presented lower values of E_{VB-max} (0.89 eV) and E_{VB-min} (-0.616).
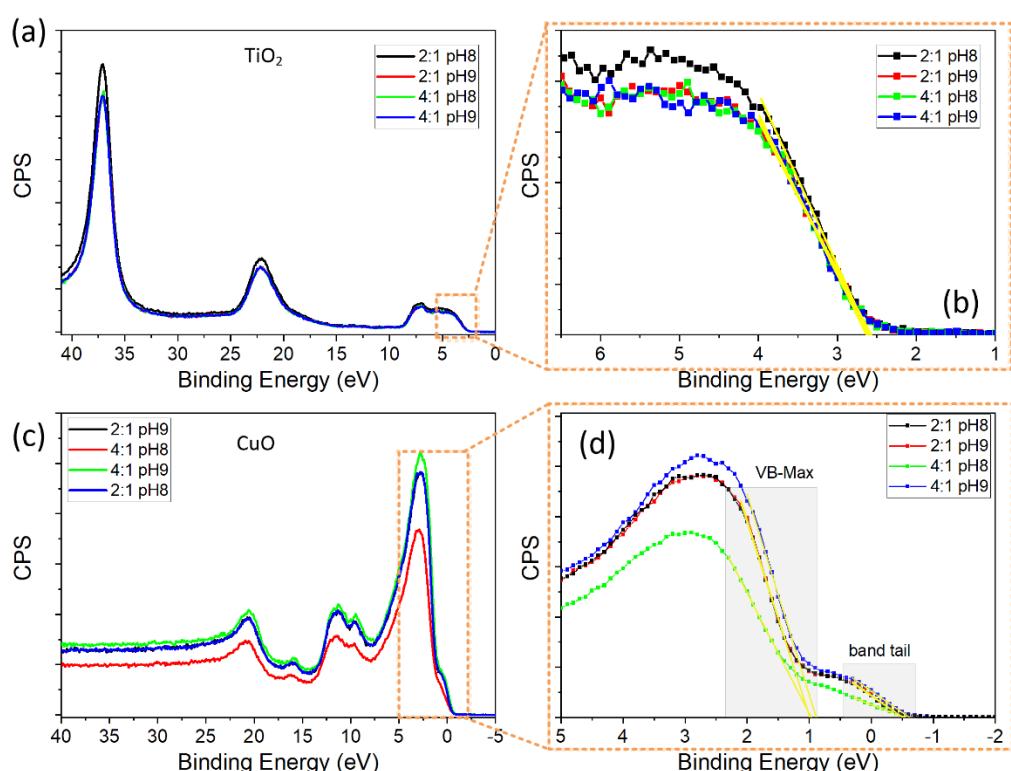

Figure 10. XPS spectra of (a) TiO_2 and (c) CuO powders taken around a low-binding energy region. (b) and (c) are the XPS valence band spectra of the oxides extracted from (a) and (c), respectively.

From the E_g and E_{VB} values previously estimated, we calculate the conduction band energy (E_{CB}) ($E_{CB} = E_{VB} - E_g$ [62]), values that are listed in Table 1. Thus, we have the full information of the energy bands of our powders. According to Table 1, all TiO_2 powders have a similar E_{CB}, of around -0.58 eV, a value that is lower than that found in most of the CuO powders (~ -0.51 eV). Similar to E_{VB}, the CuO powder synthesized by the 4:1 pH9 route present a lower E_{CB} (-0.62 eV). It is important to note that the values of E_{CB} for the CuO powders are slightly higher than the minimum E_{VB} and, in consequence, showing an overlapping effect between valence and conduction bands. From the electrical point of view, this overlapping induces a metal behavior in some regions placed at the grain surface of the CuO system. This metallic behavior observed at the surface of the semiconductor oxide can be used to trap photogenerated electrons, preventing a rapid electron-hole recombination, a useful mechanism to improve the photocatalytic activity of this system [63]. In Figure 11, we present a diagram of the energy bands for the TiO_2 and CuO powders synthesized by the 2:1 pH8 route, which represent the general behavior of the studied oxides.

Table 1. Values of E_g, E_{VB} and E_{CB} for all powders. The values labeled by * and ** correspond to the E_{VB-max} and E_{VB-min}, respectively, for the CuO.

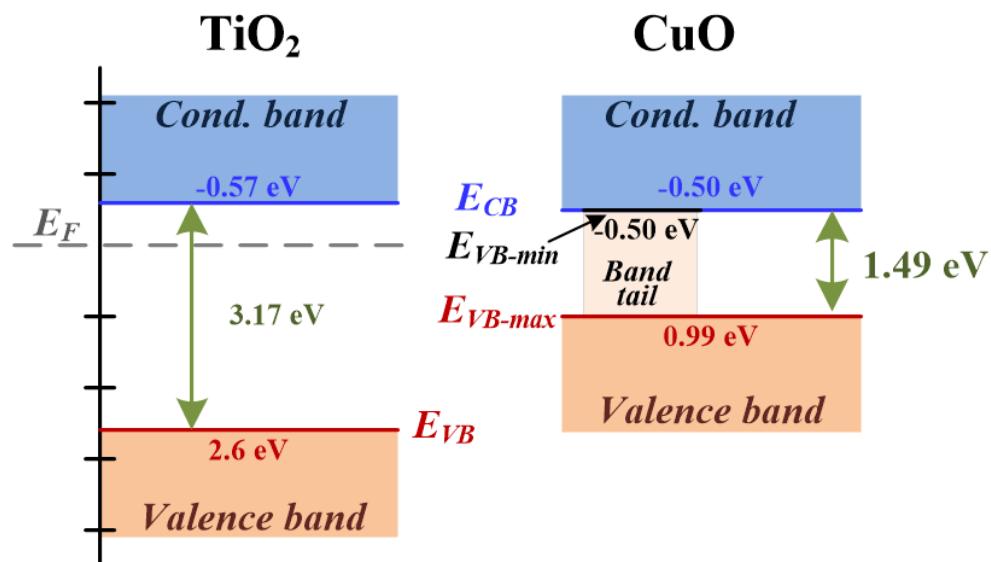| Sample	Eg (eV)	E_{VB} (eV)	E_{CB} (eV)
2:1 pH8 – TiO$_2$	3.17 ± 0.04	2.6 ± 0.1	-0.57 ± 0.07
2:1 pH9 – TiO$_2$	3.17 ± 0.03	2.6 ± 0.1	-0.57 ± 0.08
4:1 pH8 – TiO$_2$	3.18 ± 0.03	2.6 ± 0.2	-0.6 ± 0.1
4:1 pH9 – TiO$_2$	3.18 ± 0.03	2.6 ± 0.1	-0.58 ± 0.07
2:1 pH8 – CuO	1.494 ± 0.003	0.99 ± 0.06* -0.504 ± 0.005**	-0.50 ± 0.03
2:1 pH9 – CuO	1.489 ± 0.004	0.99 ± 0.05* -0.51 ± 0.01**	-0.50 ± 0.03
4:1 pH8 – CuO	1.502 ± 0.004	0.97 ± 0.03* -0.55 ± 0.01**	-0.53 ± 0.02
4:1 pH9 – CuO	1.51 ± 0.01	0.89 ± 0.07* -0.616 ± 0.005**	-0.62 ± 0.04

Figure 11. Schematic diagram of the energy bands for the TiO$_2$ and CuO powders. The values of energy levels correspond to the powders synthesized by following the 2:1 pH8 route.

4. Conclusions

High purity TiO$_2$ and CuO powders were synthesized following four Pechini-method-based synthesis routes. From the crystalline structure point of view, the variables of synthesis used in this work - the EG:CA ratio (2:1 and 4:1) and pH (8 and 9) – enabled the production of single-phase powders of the anatase TiO$_2$ and tenorite CuO systems, without the detection of secondary phases, demonstrating all routes provide the synthesis of high purity oxides in the desired phases. The microscopic analysis showed the synthesized powders are formed by grains with micrometer and submicrometer sizes; those grains with irregular shape are composed by non-compact crystallite conglomerates. In the case of TiO$_2$ powders, well-defined submicron spheres were synthesized with similar diameters in three of the synthesis routes (of around 750 nm for 2:1 pH8, 2:1 pH9 and 4:1 pH9). The high purity of the synthesized powders was also supported by FTIR experiments, where the spectra only defined the characteristic peaks of the anatase TiO$_2$ and tenorite CuO phases. In addition, the formation of a wide band around the Ti-O, Ti-O-Ti and Cu-O vibration signals indicates the powders have a nanoparticle vibratory behavior,

so that we could infer the non-compacted arrangement of nanocrystallites that form the irregular grains governs the vibrational properties of the powders.

Although the crystalline microstructure, morphological and vibrational properties of the powders did not show a clear dependency with the synthesis routes for each oxide, some differences were observed in the electronic and optical properties. While all synthesized TiO_2 powders had an Eg of approximately 3.2 eV, the optical band gap values of the CuO powders presented variations that depend on the synthesis route: the 2:1-ratio-based routes promotes a slightly lower Eg (~1.49 eV) compared to the 4:1-ratio-based one (~1.51 eV), being 2:1 pH9 the route that produces the lowest Eg (1,489 eV). Both TiO_2 and CuO powders have a direct band gap and absorb in the ultraviolet and visible regions, which is required for applications that use solar energy as an excitation source for the electronic transitions of semiconductor oxides. TiO_2 shows the maximum absorption in the ultraviolet region and decreases exponentially when entering the visible region. The 4:1 pH8 ratio shows the best response in the visible region with 50 and 28 % for the violet and red lights. The CuO powders show promising results due to their absorbance percentage are kept high along the ultraviolet and visible region, above 80%. Finally, the analysis of the XPS valence band spectra reveal the CuO powders can exhibit a hybrid metal-semiconductor behavior due to the presence of a band tail in the valence band that overlap the conduction band. This is not the case for the TiO_2 powders, where a well-defined valence band indicate a semiconductor behavior. Therefore, the synthesis routes used in this work allowed to prepare high purity TiO_2 and CuO powders with similar morphological characteristic, but they finely adjust relevant photophysical properties for the design of photovoltaic cells.

References

1. Yang, M.; He, J. Fine Tuning of the Morphology of Copper Oxide Nanostructures and Their Application in Ambient Degradation of Methylene Blue. *J. Colloid Interface Sci.* **2011**, *355*, 15–22, doi:10.1016/j.jcis.2010.11.022.
2. Zhang, Q.; Zhang, K.; Xu, D.; Yang, G.; Huang, H.; Nie, F.; Liu, C.; Yang, S. CuO Nanostructures: Synthesis, Characterization, Growth Mechanisms, Fundamental Properties, and Applications. *Prog. Mater. Sci.* **2014**, *60*, 208–337, doi:10.1016/j.pmatsci.2013.09.003.

3.   Wang, M.; Zhang, X.; Rao, R.; Qian, N.X.; Ma, Y.Q. Study on Vapor-Thermal Synthesis and Sulfur-Doping of TiO$_2$/Graphene Composites. *Appl. Surf. Sci.* **2020**, *507*, doi:10.1016/j.apsusc.2019.144856.

4.   Vargas, M.A.; Rodríguez-Páez, J.E. Amorphous TiO$_2$ Nanoparticles: Synthesis and Antibacterial Capacity. *J. Non. Cryst. Solids* **2017**, *459*, 192–205, doi:10.1016/j.jnoncrysol.2017.01.018.

5.   Crespo-Monteiro, N.; Hamandi, M.; Higuita, M.A.U.; Guillard, C.; Dappozze, F.; Jamon, D.; Vocanson, F.; Jourlin, Y. Influence of the Micro-Nanostructuring of Titanium Dioxide Films on the Photocatalytic Degradation of Formic Acid under UV Illumination. *Nanomaterials* **2022**, *12*, doi:10.3390/nano12061008.

6.   Dar, M.A.; Ahsanulhaq, Q.; Kim, Y.S.; Sohn, J.M.; Kim, W.B.; Shin, H.S. Versatile Synthesis of Rectangular Shaped Nanobat-like CuO Nanostructures by Hydrothermal Method; Structural Properties and Growth Mechanism. *Appl. Surf. Sci.* **2009**, *255*, 6279–6284, doi:10.1016/j.apsusc.2009.02.002.

7.   Rahnama, A.; Gharagozlou, M. Preparation and Properties of Semiconductor CuO Nanoparticles via a Simple Precipitation Method at Different Reaction Temperatures. *Opt. Quantum Electron.* **2012**, *44*, 313–322, doi:10.1007/s11082-011-9540-1.

8.   Vargas, M.A.; Rivera-Muñoz, E.M.; Diosa, J.E.; Mosquera, E.E.; Rodríguez-Páez, J.E. Nanoparticles of ZnO and Mg-Doped ZnO: Synthesis, Characterization and Efficient Removal of Methyl Orange (MO) from Aqueous Solution. *Ceram. Int.* **2021**, *47*, 15668–15681, doi:10.1016/j.ceramint.2021.02.137.

9.   H.J, F. *Nanomaterials: Synthesis, Properties and Applications*; 1996; ISBN 978-3527333790.

10. Ribeiro, P.C.; De Melo Da Costa, A.C.F.; Kiminami, R.H.G.A.; Sasaki, J.M.; Lira, H.L. Synthesis of TiO$_2$ by the Pechini Method and Photocatalytic Degradation of Methyl Red. *Mater. Res.* **2013**, *16*, 468–472, doi:10.1590/S1516-14392012005000176.

11. Pechini, M.P. Method of Preparing Lead and Alkaline Earth Titanates and Nobates and Coating method using the same to form a capacitor. *US Pat. 3,330,697* **1967**, 2.

12. Xu, Y.; Yuan, X.; Huang, G.; Long, H. Polymeric Precursor Synthesis of Ba2Ti9O20. *Mater. Chem. Phys.* **2005**, *90*, 333–338, doi:10.1016/j.matchemphys.2004.10.022.

13. Mashreghi, A.; Davoudi, F. The Effect of Ethylene Glycol/Citric Acid Molar Ratio in the Initial Precursor of TiO$_2$ Nanoparticle Paste Synthesized by a Polymerizable Complex Method on the Photovoltaic Properties of Dye-Sensitized Solar Cells. *Mater. Sci. Semicond. Process.* **2015**, *30*, 618–624, doi:10.1016/j.mssp.2014.11.001.

14. Hossein, M.; Morteza, A. Effect of Diverse Pechini Sol-Gel Parameters on the Size, Morphology, Structural and Optical Properties of the Tenorite (CuO) NPs: A Facile Approach for Desired Properties. *Ceram. Int.* **2020**, *46*, 17197–17208, doi:10.1016/j.ceramint.2020.03.275.

15. Shoja Razavi, R.; Reza Loghman-Estarki, M.; Farhadi-Khouzani, M.; Barekat, M.; Jamali, H. Large Scale Synthesis of Zinc Oxide Nano- and Submicro-Structures by Pechinis Method: Effect of Ethylene Glycol/Citric Acid Mole Ratio on Structural and Optical Properties. *Curr. Nanosci.* **2011**, *7*, 807–812, doi:10.2174/157341311797483745.

16. Mai, Y.J.; Wang, X.L.; Xiang, J.Y.; Qiao, Y.Q.; Zhang, D.; Gu, C.D.; Tu, J.P. CuO/Graphene Composite as Anode Materials for Lithium-Ion Batteries. *Electrochim. Acta* **2011**, *56*, 2306–2311, doi:10.1016/j.electacta.2010.11.036.

17. Narayanan, M.; Vigneshwari, P.; Natarajan, D.; Kandasamy, S.; Alsehli, M.; Elfasakhany, A.; Pugazhendhi, A. Synthesis and Characterization of TiO$_2$ NPs by Aqueous Leaf Extract of Coleus Aromaticus and Assess Their Antibacterial, Larvicidal, and Anticancer Potential. *Environ. Res.* **2021**, *200*, 111335, doi:10.1016/j.envres.2021.111335.

18. Lan, Y.; Lu, Y.; Ren, Z. Mini Review on Photocatalysis of Titanium Dioxide Nanoparticles and Their Solar Applications. *Nano Energy* **2013**, *2*, 1031–1045, doi:10.1016/j.nanoen.2013.04.002.

19. Kohtani, S.; Yoshioka, E.; Miyabe, H. Photocatalytic Hydrogenation on Semiconductor Particles. In *Hydrogenation*; InTech, 2012; Vol. 11, p. 13 ISBN 0000957720.

20. Diamanti, M. Special Issue: Novel Photoactive Materials. *Materials (Basel).* **2018**, *11*, 2553, doi:10.3390/ma11122553.

21. Valencia, S.; Marín, J.M.; Restrepo, G. Study of the Bandgap of Synthesized Titanium Dioxide Nanoparticules Using the Sol-Gel Method and a Hydrothermal Treatment. *Open Mater. Sci. J.* **2010**, *4*, 9–14, doi:10.2174/1874088X01004020009.

22. Reddy, K.M.; Manorama, S. V.; Reddy, A.R. Bandgap Studies on Anatase Titanium Dioxide Nanoparticles. *Mater. Chem. Phys.* **2003**, *78*, 239–245, doi:10.1016/S0254-0584(02)00343-7.

23. Kuznetsov, V.N.; Serpone, N. Visible Light Absorption by Various Titanium Dioxide Specimens. *J. Phys. Chem. B* **2006**, *110*, 25203–25209, doi:10.1021/jp064253b.

24. Hossain, F.M.; Sheppard, L.; Nowotny, J.; Murch, G.E. Optical Properties of Anatase and Rutile Titanium Dioxide: Ab Initio Calculations for Pure and Anion-Doped Material. *J. Phys. Chem. Solids* **2008**, *69*, 1820–1828, doi:10.1016/j.jpcs.2008.01.017.

25. Wang, Y.; Lany, S.; Ghanbaja, J.; Fagot-Revurat, Y.; Chen, Y.P.; Soldera, F.; Horwat, D.; Mücklich, F.; Pierson, J.F. Electronic Structures of Cu2O, Cu4O3, and CuO: A Joint Experimental and Theoretical Study. *Phys. Rev. B* **2016**, *94*, 1–10, doi:10.1103/PhysRevB.94.245418.

26. Heinemann, M.; Eifert, B.; Heiliger, C. Band Structure and Phase Stability of the Copper Oxides Cu$_2$O, CuO, and Cu$_4$O$_3$. *Phys. Rev. B - Condens. Matter Mater. Phys.* **2013**, *87*, 3–7, doi:10.1103/PhysRevB.87.115111.

27. Tamayo, K.; Marín, L.; Gross, K.; Amaya, C.; Reyes, D.; Lopera, W.; Gómez, M. Influence of thermal annealing on the structural and optical properties of nanostructures based on copper oxides. *Ingenieria y Competitividad* **2022**, 24.

28. Vargas, M.A.; Franco, Y.; Ochoa, Y.; Ortegón, Y.; Rodriguez Paez, J.E. TiO$_2$ sintetizado por el método de Precursor Polimérico (Pechini): Estructura de la resina intermedia. *Bol. la Soc. Esp. Ceram. y Vidr.* **2011**, *50*, 267–272, doi:10.3989/cyv.352011.

29. Joni, I. M.; Nulhakim, L.; Panatarani, C. Characteristics of TiO$_2$ particles prepared by simple solution method using TiCl3 precursor. *J. Phys.: Conf. Ser.* **2018**, 1080, 012042, doi :10.1088/1742-6596/1080/1/012042.

30. Kim, N. Y.; Lee, H. K.; Moon, J. T.; Joo, J. B. Synthesis of Spherical TiO$_2$ Particles with Disordered Rutile Surface for Photocatalytic Hydrogen Production. *Catalysts* **2019**, 9, 491, doi:10.3390/catal9060491.

31. Cai, W.; Yang, H.; Guo, X. A Facile Synthesis of Nanocrystalline Spherical TiO$_2$ Particles and its Photoluminescent Properties. *Procedia Eng.* **2014**, 94, 71 – 75, doi:10.1016/j.proeng.2013.11.042.

32. Pal, M.; García-Serrano, J.; Santiago, P.; Pal, U. Size-Controlled Synthesis of Spherical TiO$_2$ Nanoparticles: Morphology, Crystallization, and Phase Transition. *J. Phys. Chem. C* **2007**, 111, 96-102, doi:10.1021/jp0618173.

33. Fazio, G.; Ferrighi, L.; Di Valentin, C. Spherical vs Faceted Anatase TiO$_2$ Nanoparticles: A Model Study of Structural and Electronic Properties. *J. Phys. Chem. C* **2015**, 119, 35, 20735–20746, doi: 10.1021/acs.jpcc.5b06384.

34. Tellez, L.; Rubio, F.; Peña, R.; Rubio, J. Seguimiento por espectroscopia infrarroja (FT-IR) de la copolimerizacion de TEOS (tetraetilortosilicato) y PDMS (polidimetilsiloxano) en presencia de TBT (tetrabutiltitanio). *Bol. Soc. Esp. Ceram*. **2004**, 43 [5] 883-890

35. Guzmán, A.; Fernandez, A.; Rodriguez, J. Estudio de las reacciones de hidrólisis y condensación del titanio en presencia de acetilacetona. *Rev. Acad. Colomb. Cienc*. **2007**, Vol 31[121], 529-536.

36. Nakamoto, K. *Infrared and Raman Spectra of Inorganic and Coordination Compounds*. Ed. John Wiley & Sons, New York, **1997**.

37. Praveen, P.; Viruthagiri, G.; Mugundan, S.; Shanmugam, N. Structural, optical and morphological analyses of pristine titanium di-oxide nanoparticles-Synthesized via sol-gel route. *Spectrochim. Acta A: Mol. Biomol. Spectrosc.* **2014**, 117, 622-629, doi:10.1016/j.saa.2013.09.037.

38. Rashidzadeh, M. Synthesis of High-Thermal Stable Titanium Dioxide Nanoparticles. *Int. J. Photoenergy* **2008**, 4 pages, doi:10.1155/2008/245981.

39. Ba-Abbad, M. M.; Kadhum, A. A.; Mohamad, A. B.; Takriff, M. S.; Sopian, K. Synthesis and Catalytic Activity of TiO$_2$ Nanoparticles for Photochemical Oxidation of Concentrated Chlorophenols under Direct Solar Radiation. *Int. J. Electrochem. Sci.* **2012**, 7, 4871 – 4888.

40. Gohari, G.; Mohammadi, A.; Akbari, A.; Panahirad, S.; Reza Dadpour, M.; Fotopoulos, V.; Kimura, S. Titanium dioxide nanoparticles (TiO$_2$ NPs) promote growth and ameliorate salinity stress effects on essential oil profile and biochemical attributes of Dracocephalum moldavica. *Scientific Reports* **2020,** 10, 912, doi:0.1038/s41598-020-57794-1.

41. Bagheri, S.; Shameli, K.; Abd Hamid, S. B. Synthesis and Characterization of Anatase Titanium Dioxide Nanoparticles Using Egg White Solution via Sol-Gel Method. *Composite Nanoparticles* **2013**, doi:10.1155/2013/848205.

42. Yu, J.; Su, Y.; Cheng, B.; Zhou, M. Effects of pH on the microstructures and photocatalytic activity of mesoporous nanocrystalline titania powders prepared via hydrothermal method. *J. Mol. Catal. A: Chem.* **2006,** 258, Issues 1–2, 104-112, doi:10.1016/j.molcata.2006.05.036.

43. Al-Amin, M.; Chandra Dey, S.; Ur Rashid, T.; Ashaduzzaman, Md.; Shamsuddin, S. Md. Solar Assisted Photocatalytic Degradation of Reactive Azo Dyes in Presence of Anatase Titanium Dioxide. *IJLRT* **2016**, 2 (3), 14-21.

44. Adnan Ouda, A.; Mohamad Alosfur, F. K.; Ridha, N. J.; Abud, S. H.; Umran, N. M.; Al-aaraji, H. H.;   Madlool, R. A. Facile method to synthesis of anatase TiO$_2$ nanorods. *J. Phys.: Conf. Ser.* **2018**, 1032, 012038, doi:10.1088/1742-6596/1032/1/012038.

45. Sethi, D.; Sakthivel, R. ZnO/TiO$_2$ composites for photocatalytic inactivation of Escherichia coli. *J. Photochem. Photobiol. B: Biol.* **2017**, 168, 117-123, doi:10.1016/j.jphotobiol.2017.02.005.

46. Azam, A.; Ahmed, A.S.; Oves, M.; Khan, M.; Memic, A. Size-dependent antimicrobial properties of CuO nanoparticles against Gram-positive and-negative bacterial strains. *Int. J. Nanomed* **2012**, 7, 3527-3525, doi:10.2147/IJN.S29020.

47. Elango, M.; Deepa, M.; Subramanian, R.; Mohamed Musthafa, A. Synthesis, Characterization, and Antibacterial Activity of Polyindole/Ag–Cuo Nanocomposites by Reflux Condensation Method. *Polym-Plast Technol Eng* **2018**, 57(14), 1440-1451, doi:10.1080/03602559.2017.1410832.

48. Stefan, M.; Pana, O., Leostean, C.; Bele, C.; Silipas, D.; Senila, M.; Gautron, E. Synthesis and characterization of Fe$_3$O$_4$–TiO$_2$ core-shell nanoparticles. *J. Appl. Phys* **2014**,116, 114312, doi:10.1063/1.4896070.

49. Le, Yuan L.; Weng, X.; Zhou, M.; Zhang, Q.; Deng, L. Structural and Visible-Near Infrared Optical Properties of Cr-Doped TiO$_2$ for Colored Cool Pigments.*Nanoscale Res Lett*. **2017**, 12, 597, doi:10.1186/s11671-017-2365-5.

50. Escobedo Morales, A.; Sanchez Mora, E.; Pal, U. Use of diffuse reflectance spectroscopy for optical characterization of un-supported nanostructures. *Rev. Mex. Fís. S* **2007** 53 (5) 18–22.

51. Weizhong, J.; Ying, W.; L Gu. Influence of TiO$_2$ film on photo-catalytic property of enamels. *J. Non. Cryst. Solids* **2007**, 353,44-45, 4191–4194, doi:10.1016/j.jnoncrysol.2007.06.072.

52. Puzenat, E. Photocatalytic self-cleaning materials: Principles and impact on atmosphere. *EPJ* 1 **2009**, 69–74. doi:10.1140/epjconf/e2009-00911-2.

53. Fernandes Machado, N. R. C.; Santana, V. Influence of thermal treatment on the structure and photocatalytic activity of TiO$_2$ P25. *Catalysis Today*   **2005**, 107u108, 5955601, doi:10.1016/j.cattod.2005.07.022.

54. Sawicka-Chudy, P.; Sibiński, M.; Wisz, G.; Rybak-Wilusz, E.; Cholewa M. Numerical analysis and optimization of Cu_2O/TiO_2, CuO/TiO_2, heterojunction solar cells using SCAPS. *J. Phys: Conf. Ser.* **2018,** 1033, 012002, doi:10.1088/1742-6596/1033/1/012002.

55. X-ray Photoelectron Spectroscopy (XPS) Reference Pages. Available online: www.xpsfitting.com (accessed on 07 March 2022).

56. Biesinger, M.C. Advanced analysis of copper X-ray photoelectron spectra. *Surf. Interface Anal.* **2017**, doi: 10.1002/sia.6239.

57. Ghijsen, J.; Tjeng, L. H.; Van Elp, J.; Eskes, H.; Westerink, J.; Sawatzky, G. A.; Czyzyk, M. T. Electronic structure of Cu_2O and CuO. *Phys. Rev. B* **1988**, 38, 11322.

58. Wang, Y. Controllable growth, microstructure and electronic structure of copper oxide thin films. Other. Université de Lorraine, **2015**.

59. Hussain, M.; Ibupoto, Z. H.; Abbassi, M. A.; Khan, A.; Pozina, G.; Nur, O.; Willander, M.. Synthesis of CuO/ZnO composite nanostructures, their optical characterization and valence band offset determination by x-ray photoelectron spectroscopy. *J. Nanoelectron. Optoelectron* **2014**, 9, 1-9, doi:10.1166/jno.2014.1594.

60. Galakhov, V. R.; Finkelstein, L. D.; Zatsepin, D. A.; Kurmaev, E. Z.; Samokhvalov, A. A.; Naumov, S. V.; Tatarinova, G. K. Interaction of Cu 3d and O 2p states in $Mg_{1-x}Cu_xO$ solid solutions with NaCl structure: X-rayphotoelectron and x-ray emission study. *Phys. Rev. B.* **2000**, 62, 8.

61. Ansari, S. A.; Cho, M. H. Highly Visible Light Responsive, Narrow Band gap TiO_2 Nanoparticles Modified by Elemental Red Phosphorus for Photocatalysis and Photoelectrochemical Applications. *Scientific Reports* **2016**, 6, 25405, doi:10.1038/srep25405.

62. Arif Khan, M.; Nayan, N.; Shadiullah; Ahmad, M. K.; Fhong Soon C. Surface Study of CuO Nanopetals by Advanced Nano-characterization Techniques with Enhanced Optical and Catalytic Properties. *Nanomaterials* **2020**, 10(7), 1298, doi:10.3390/nano10071298.

63. Feng, N.; Liu, F.; Huang, M.; Zheng, A.; Wang, Q.; Chen, T.; Cao, G.; Xu, J.; Fan, J.; Deng, F. Unravelling the Efficient Photocatalytic Activity of Boron-induced Ti^{3+} Species in the Surface Layer of TiO_2. *Scientific Reports* **2016**, 6, 34765, doi: 10.1038/srep34765.